Case Studies in Thermal Engineering 53 (2024) 103888

Contents lists available at ScienceDirect

Case Studies in Thermal Engineering

journal homepage: www.elsevier.com/locate/csite

Oblique microchannel merged with circle micro pin-fin as a novel hybrid heat sink for cooling of electronic devices

Yousef Alihosseini [a,b,c,1], Yaser Oghabneshin [c,1], Amir Rezazad Bari [c], Sahel Moslemi [d], Mohammad Zabetian Targhi [c,*], Wei Guo [a,b], Amirarsalan Mashhadian [e]

[a] Mechanical Engineering Department, FAMU-FSU College of Engineering, Florida State University, Tallahassee, FL, 32310, USA
[b] National High Magnetic Field Laboratory, 1800 East Paul Dirac Drive, Tallahassee, FL, 32310, USA
[c] Mechanical Engineering Department, Tarbiat Modares University, Tehran, Iran
[d] Chemical Engineering Department, Sahand University of Technology, Tabriz, Iran
[e] Department of Mechanical Engineering, The University of Texas at Dallas, Richardson, TX, 75080, USA

GRAPHICAL ABSTRACT

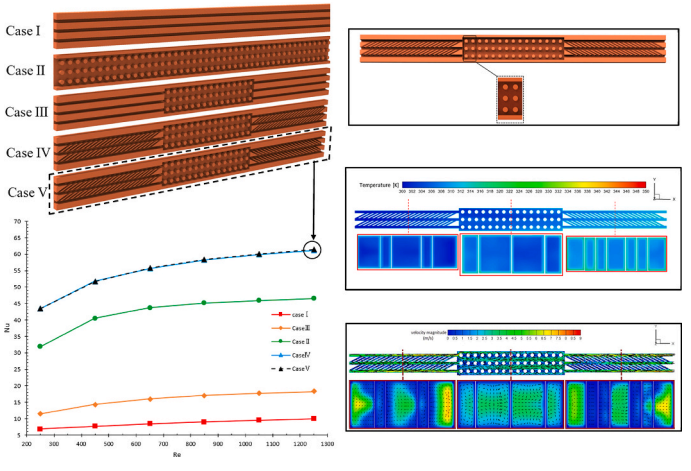

* Corresponding author.
E-mail address: zabetian@modares.ac.ir (M. Zabetian Targhi).
[1] These authors contributed equally: Yousef Alihosseini and Yaser Oghabneshin.

https://doi.org/10.1016/j.csite.2023.103888
Received 28 June 2023; Received in revised form 27 November 2023; Accepted 6 December 2023
Available online 9 December 2023

ARTICLE INFO

Keywords:
Microchannel heat sink
Hybrid pattern
Heat transfer
Performance evaluation criteria
Electronic cooling
Hotspot creation

ABSTRACT

Recently, the advantages of microchannel and micro pin-fin heat sinks for cooling have become clear. This study delves into the effects of hybrid designs on electronic chip cooling by combining microchannel and pin-fin patterns. The research contrasts the performance of a straight microchannel heat sink (Case I), circular pin-fin (Case II), straight-circular pin-fin-straight (Case III), and oblique grooved straight-circular pin-fin-oblique grooved straight (Case IV). Results show that Case IV's *Nu* number reaches 61 at $Re = 1250$, surpassing Case I, Case II, and Case III by 517 %, 32 %, and 235 %, respectively. Case IV also has the highest pressure drop. The study calculates each Case's performance evaluation index (η), highlighting the balance between enhanced *Nu* numbers and pressure drops. Case IV's η is notably higher than Case II and Case III. To achieve a more uniform thermal distribution across the entire heat sink, the orientation of the oblique grooves is modified in Case IV, resulting in a new design labeled Case V. While Cases IV and V have similar Nusselt numbers, Case V's design ensures consistent temperature distribution, reducing hotspot risks on the chip.

1. Introduction

Thermal engineers always strive to design better models to control heat generation challenges in electronic devices, increasing device efficiency [1,2]. Tuckerman and Pease were pioneers in proposing using single and multi-phase microchannel heat sinks (MCHS) to amplify the surface-to-volume ratio [3,4] to increase the surface-to-volume ratio. Since then, various novel ideas have been proposed to improve considerably the performance of MCHS. Broadly, the factors influencing MCHS efficiency can be categorized into two groups: (a) properties of the working fluid and (b) heat sink geometry parameters [5,6]. Many studies have been conducted regarding working fluids in the past decades. It has been found that working fluid involving boiling, nanoparticles, and Phase Change Material (PCM) could effectively enhance the MCHS performance [7,8]. Besides, geometric parameters related to the heat sink pattern, the cross-section shape, and the manifolds have been widely investigated [9,10].

In particular, Khoshvaght-Aliabadi and Nozan [11] investigated three corrugated mini-channel heat sinks and compared their performance with the straight heat sink. Their results showed that the boundary layer disruption inside the corrugated shape was more effective than the straight Case arising from the fluid recirculation. Due to the swirl flows generated inside the trapezoidal corrugation, the highest performance enhancement of trapezoidal mini channels was found. The sinusoidal wavy pattern has also gained attention among various periodic designs for its superior performance [12]. Recent studies have delved into diverse pin-fin patterns [13,14]. Pin-fins induce fluid mixing and secondary flows, enhancing the heat sink's performance. Hasan [15] investigated different cross-sections of micro pin-fin heat sinks. Their results revealed that circular fins have the maximum heat transfer capability. The performance of circular, square, and hexagonal pin-fins was analyzed systematically by Tehmina Ambreen et al. [16]. Their study found the maximum Nusselt number of 10 for circular fins. The minor separation region in circular pin-fins was investigated, which was the cause of the enhanced thermal performance [17]. Duangthongsuk et al. [18] conducted experimental research on circular and square pin fins' hydraulic and thermal effects in heat sinks. Their findings indicated that circular pin-fin heat sinks outperformed square ones by approximately 9 % in thermal efficiency. This increase can be explained by the flow-guided structures of the circular pin-fin heat sink. The square cross-section has more pressure drop due to the sharp points and narrowest distance between the adjacent square pin fins.

Lee et al. [19] numerically studied a new pattern introducing oblique grooves into conventional channels. With an oblique angle of 27°, a fin and channel width of 100 μm, and fin pitches of 300 μm, they observed an increase in both average and local heat transfer coefficients. This increase was primarily attributed to the disruption of the thermal boundary layer and the creation of secondary flows. Compared to the conventional design, the heat transfer coefficient at the upstream differed by 27.62 %, while in the middle and at the channel's end, it was 105.9 % and 102.09 %, respectively. The pressure drop in the oblique microchannel was negligible compared to the conventional design. In the other study conducted by Lee et al. [20], they have conducted empirical studies on the oblique, rectangular microchannel. This design featured a 25 × 25 mm footprint, channel widths of 500 μm and 300 μm, fin widths of 465.2 μm and 245.2 μm, and pitch fin widths of 1995.2 μm and 1164.5 μm, all examined within a Reynolds range of 300–800. They compared the heat transfer and pressure drop with the conventional form of each one. The findings showed that the heat transfer rate and pressure drop in both dimension sets were more than conventional. However, by presenting the E_{Nu} and E_f parameters, they observed that the heat transfer rate to pressure drop was much higher in Reynolds of 500. The fluid flow and heat transfer in the oblique microchannel with fin widths of 100 μm and 200 μm, and in pitches of 400 μm, 800 μm, and 1500 μm, and fin angles of 15°, 27°, and 45° were studied by by the same research group [21]. The overall footprint was 12.7 × 12.7 mm, examined in the Reynolds range of 180–680 and heating power of 273 W. Due to the secondary flow and the re-development of the thermal boundary layer in each fin, the heat transfer coefficient in the oblique microchannel increased. The rate of heat transfer at a fixed pressure drop was in a way that the microchannel with a width of 100 μm, and pitch of 400 μm, and a degree of 27° had the most heat transfer, while the microchannel with a width of 200 μm, and pitch of 800 μm and a degree of 45° had the minor heat transfer coefficient. Alihosseini et al. [6] introduced a novel MCHS design that combined oblique grooved fins with a wavy pattern. Their results illustrated that a hybrid of oblique grooved fins and the wavy pattern was more efficient than a simple wavy one because the secondary flow was generated in the hybrid Case, and it caused a rise in the heat transfer rate. Also, the area wetted was increased, thereby increasing the *Nu* number.

Based on the literature review, both oblique MCHS and circular micro pin-fin (MPF) patterns are frequently utilized due to their enhanced efficiency. Since little attention has been paid to combining the two patterns, a gap in the combination of two patterns was felt. Therefore, this study investigates the combined use of MCHS and MPF to enhance cooling efficiency. In this regard, five patterns are proposed for more evaluation, including (a) Straight (Case I), (b) Pin-Fin (Case II), (c) Straight-Circular Pin-Fin-Straight (Case III), (d) Oblique MCHS-Circular Pin-Fin-Oblique MCHS (Case IV), and (e) Oblique MCHS-Circular Pin-Fin-Oblique star (Case V). For Case V, the downstream oblique grooves are oriented opposite to those upstream. In this paper, Sections 2 and 3 detail the geometrical design, governing equations, and principles of numerical simulation for MCHS. Section 4 presents results, focusing on selecting the optimal MCHS pattern based on Thermo-Hydraulic performance.

2. Geometry design

This study assesses the performance of five distinct MCHS designs. Fig. 1 provides a 3D schematic view of these patterns, and Table 1 shows a detailed description of these designs. As depicted in Fig. 1, Case I features three parallel straight channels, with a length of 25 mm and a hydraulic diameter of 280 μm. In contrast, Case II includes three inline 45-pin-fin arrays with a pin-fin diameter of 280 μm. It should be noted that Case III and Case I are references based on which combined models would be developed. The three other designs are developed by innovatively combining straight microchannels, grooves, and pin-fins. The Case III combines straight microchannels and pin-fins, in which three straight microchannels surrounded the pin-fins at the two ends. Case IV involves a grooved design with a groove width of 375 μm surrounded by pin-fins. Finally, Case V is the same as Case IV, except that the groove direction in the outlet is opposite to the inlet groove direction. Since the models are symmetric, a minimum of three channels could be studied to efficiently simulate and evaluate the entire model while reducing the computation time and cost.

The painstaking details concerning the dimensions are shown in Fig. 2. It is noteworthy that the dimensions and geometries were extracted from Alihosseini and Ghorbani as they maximized thermal performance [22,23].

When comparing Case I and Case II designs, it was evident that Case II had superior performance. A combination of Case I and Case II was examined to enhance heat sink performance. Pin-fins were positioned in the center of channel, as placing them in the middle third could lead to a more efficient flow breakdown and reduced development length. However, it was found that Case III had lower thermal performance than Case II. Based on the literature reports, diagonal grooves were applied to the straight microchannel with 375 μm pitches to enhance overall heat sink performance to develop the Case IV and Case V designs. The developed models maximized thermal performance since the grooves made a larger contribution than micro-pin-fins to the heat sink. Additionally, to ensure uniform temperature and flow distribution across the heat sink, grooves oriented in the opposite direction were employed in the outlet of the heat sink.

3. Numerical methods

The finite volume method (FVM) is used in ANSYS Fluent V.21 to implement simulations and solve solid and liquid heat transfer equations simultaneously. Also, the SIMPLE algorithm is employed to couple the velocity and pressure [24,25]. The momentum and energy equations are discretized using the second-order upwind scheme, whereas the second-order upwind scheme is utilized to discretize the pressure equation through the standard approach. To simultaneously solve the flow and heat transfer, three-dimensional simulations are performed by assuming convective heat transfer for the fluid in the microchannel and conductive heat transfer in the solid copper part. The simulation assumptions included [26,27].

(1) Laminar steady-state flow
(2) Incompressible fluid
(3) Constant thermophysical properties of the cooling fluid. Since the difference between the input and output temperatures was found to be 9 °C, the thermophysical properties of the fluid could be assumed to remain unchanged, neglecting their temperature-dependent variations.
(4) Negligible viscous losses

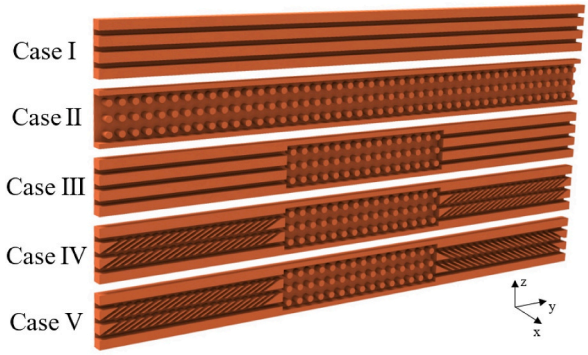

Fig. 1. A schematic view of five considered cases.

Table 1
The descriptions related to five considered cases.

Models	Description
Case I	a straight microchannel heat sink
Case II	circular pin-fin
Case III	straight-circular pin-fin-straight
Case IV	oblique grooved straight-circular pin-fin-oblique grooved straight
Case V	oblique grooved straight-circular pin-fin-oblique grooved straight reversed

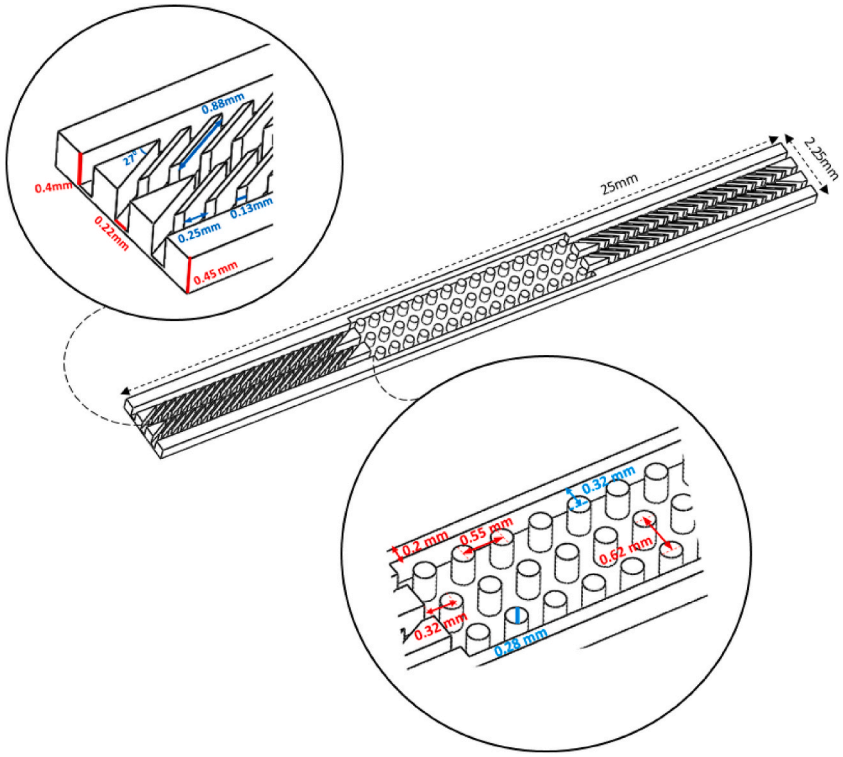

Fig. 2. The dimension of simulated geometry.

The assessment of the flow regime hinges on the Reynolds number at the microchannel heat sinks' inlet. In the critical regions, the Reynold number calculated by the maximum velocity is considered 2200 as a critical Reynold, mentioned by Chapman et al. [28] for determining laminar flow. Therefore, all assumptions about laminar flow are checked. For instance, the maximum velocity occurred near the Case IV outlet at *Re* 1250. The calculated Reynolds number in this region is 1160, which is less than the critical amount.

According to the above assumptions, the governing equations are written as follows [29,30]:

Conservation of mass:

$$\rho_f \nabla . \left(\overrightarrow{U} \right) = 0 \tag{1}$$

Momentum equation:

$$\rho_f \left(\overrightarrow{U} . \nabla \right) \overrightarrow{U} = -\nabla p + \mu \, \nabla^2 \overrightarrow{U} \tag{2}$$

Liquid energy equation:

$$\rho_f \, C_{pf} \left(\overrightarrow{U} . \nabla T \right) = \nabla . \left[k_f \nabla T \right] \tag{3}$$

Solid energy equation:

$$\nabla . \left[k_s \nabla T \right] = 0 \tag{4}$$

In the given equations, U, P, ρ_f, μ, C_{pf}, and k_f are the velocity vector, the pressure, the fluid density, dynamic viscosity, specific heat, and thermal conductivity, respectively. Furthermore, k_s is the solid thermal conductivity.

The local temperature of the fluid is obtained as:

$$T_{f,x} = \frac{\int_{A_c} \rho_f u C_{p_f} T \, dA_c}{\int_{A_c} \rho_f u C_{p_f} \, dA_c} \tag{5}$$

The average local temperature of the microchannel wall is calculated as:

$$T_{w,x} = \frac{1}{w} \int_{w} T_w \, dw \tag{6}$$

The local heat transfer coefficient is given by:

$$h_x = \frac{q'' A_b}{\left(T_{\omega,x} - T_{f,x}\right) A_i} \tag{7}$$

In this equation, while q″, A_b, and Ai are the heat flux, the base area of the channel that the heat flux applied to it, and the fluid-solid interface area that the coolant removes the heat from it respectively, $T_{w,x}$ and $T_{f,x}$ are the local wall temperature and the local fluid bulk temperature.

The local and average Nusselt numbers in the microchannel are given by:

$$Nu_x = \frac{h_x D_h}{k_f} \tag{8}$$

$$Nu = \frac{1}{L} \int_{L} Nu_x \, dx \tag{9}$$

Where L is the length of the channel, k_f is the fluid thermal conductivity and D_h is the channel hydraulic diameter that is defined by:

$$D_h = \frac{4A_{ch}}{P} \tag{10}$$

Where A_{ch} and P are the cross-section and perimeter of the channel inlet plenum, respectively. The pressure drop and friction coefficient are obtained as follows:

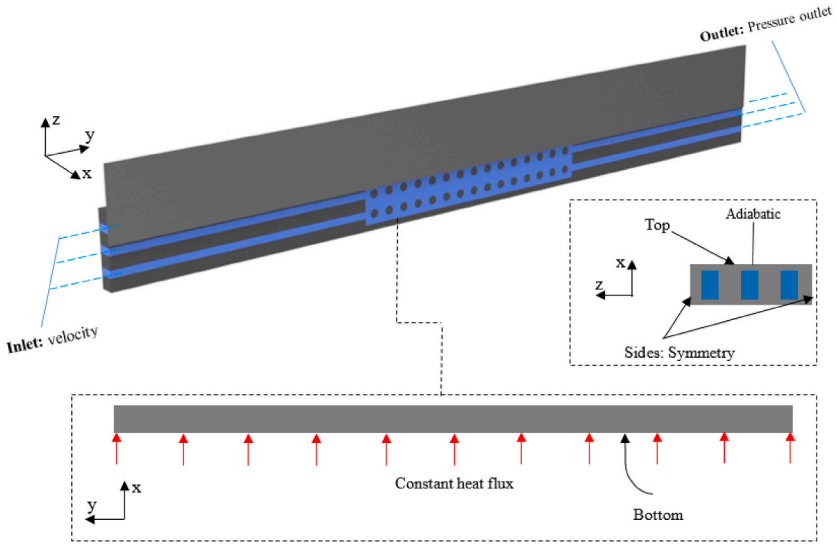

Inlet: $V_x = V_y = 0$, $Vz = V_{in}$ & $T = T_{in}$

Bottom: $V_x = V_y = Vz = 0$, $q = constant$

Outlet: $P_{out} = P_{atm}$

Top: *Adiabatic*

sides: *Symmetry*

Fig. 3. Boundary conditions and computational domain.

$$\Delta P = P_{in} - P_{out} \tag{11}$$

$$f = \frac{2\,\Delta P\,D_h}{\rho_f L\,U^2} \tag{12}$$

3.1. Boundary conditions

The boundary conditions are set based on the literature on commercialized microchannel heat sinks. The input velocity of the microchannel is assumed to be uniform, with an input temperature of 300 K. The output pressure is set to atmospheric pressure. A fixed heat flux of 80 W/cm^2 is applied to the bottom surface of the microchannel, while the top surface is assumed to be adiabatic. The boundary condition at the side walls is considered as symmetrical. Moreover, the fluid and solid body are assumed to have the same velocity in the solid-liquid interface, and the conservation of heat flux is implemented. Also, the fluid velocity would be zero on the internal walls, based on the no-slip condition. Fig. 3 shows a schematic view of the boundary conditions.

Distilled water is applied as the cooling fluid due to its high thermophysical properties, abundance, and wide use in scientific and commercial applications. Copper, moreover, is used as the heat sink material due to its high conductivity. Table 2 reports the thermophysical properties of water and copper [31].

3.2. Grid independence

To evaluate the grid independency, four structured grids, a total of nearly 10^6, 2×10^6, 3×10^6, and 4×10^6 elements, were studied using the Meshing Module in *ANSYS Fluent V.21* Finer grids were used in the vicinity of walls due to larger temperature and velocity gradients, as shown in Fig. 4. Fig. 5 plots the local Nusselt number versus the dimensionless microchannel length (i.e., the main performance evaluation index of a heat exchanger) for Case III to compare the grids. As can be seen, the first grid with 10^6 had a larger error than the other grids, and the local Nusselt number showed almost the same trend in the three other grids; the second and third grids had maximum differences of nearly 7.5 % and 1.3 % from the fourth one at $x' = 0.4$, respectively. Hence, the grid with 3×10^6 elements was utilized to proceed with the simulations at the optimal computation time and cost. According to Fig. 5, the fluid temperature increases in the straight channel as the cooling fluid flows, and the local Nusselt number and, thus, heat transfer decline as the thermal boundary layer grows. At the beginning of the circular pin-fins ($x' = 0.3$–0.4), flow mixing rises due to a sharp change in the cross-sectional area and the appearance of barriers, leading to a jump of a good slope in the local Nusselt number in the interface of the straight and pin-fin inlet. Then, the local Nusselt number reduces as the fluid flows through the pin fins. The solid fins make a more considerable contribution at $x' = 0.5$ (precisely in the middle of the heat sink) than at $x' = 0.4$ and $x' = 0.6$. Thus, the local Nusselt number undergoes a significant reduction at $x' = 0.5$. The Nusselt number saw considerable growth at $x' = 0.6$, which stems from the sharp decrease in the cross-sectional area in the interface of the pin-fin outlet and straight channel, leading to increased flow mixing. Eventually, the Nusselt number reduces, along with increased temperature and decreased cooling, as the fluid flows through the straight microchannel toward the outlet.

3.3. Validation

To validate the proposed numerical framework, the straight model was compared to the experimental data of Sui et al. work [32]. Fig. 6 compares the average Nusselt numbers and friction coefficients. As can be seen, the numerical and experimental results are in acceptable agreement, regardless of the Reynolds number. At a Reynolds number of 300, the maximum discrepancies observed between the numerical and experimental values were approximately 6.5 % for the Nusselt numbers and 7.4 % for the friction coefficients. Considering that 8–15 % uncertainty for the Nusselt number and 3 % uncertainty for the friction coefficient in the experimental results are reasonable, the validity of the proposed numerical models can be ensured.

4. Results and discussion

In the present work, five novel three-dimensional models were simulated to monitor the flow and heat transfer. The parameters of microchannel heat sinks, i.e., the pressure drop and Nusselt number, were studied to evaluate thermal performances and identify the most efficient heat sink design. The system of a copper microchannel and a water flow was simulated at Reynolds numbers of 250–1250 (an increment interval of 200) at a fixed input heat flux of 80 W/cm^2.

4.1. Heat transfer

Fig. 7 illustrates the impact of geometric design on heat transfer by plotting the Nusselt number against the Reynolds number, a crucial metric for evaluating heat sink performance. According to Fig. 7, the Nusselt number variation rates of the proposed models were found to be larger than that of the base model (i.e., Case I) at Reynolds numbers below 650. However, the variation rates become smaller at Reynolds numbers higher than 650. In particular, the increasing Nusselt number of Case V, Case IV, Case II, and Case III were

Table 2
Thermo-physical properties of water and copper [31].

Material	Density (kg/m^3)	Specific Heat Capacity (J/kg. K)	Thermal Conduction Coefficient (W/m. K)	Viscosity (kg/m. s)
Distilled water	998	4184	0.6	0.0010013
Copper	8933	384	401	–

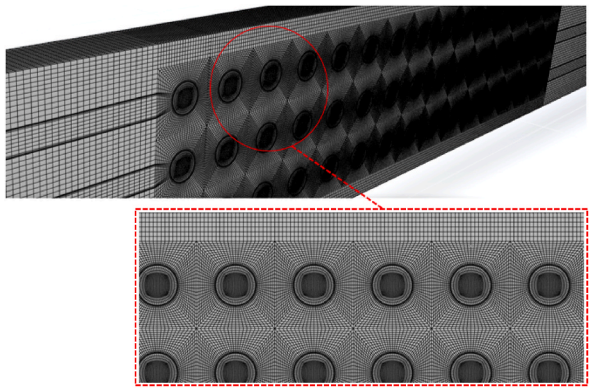

Fig. 4. Cells applied to discretize the computational domain.

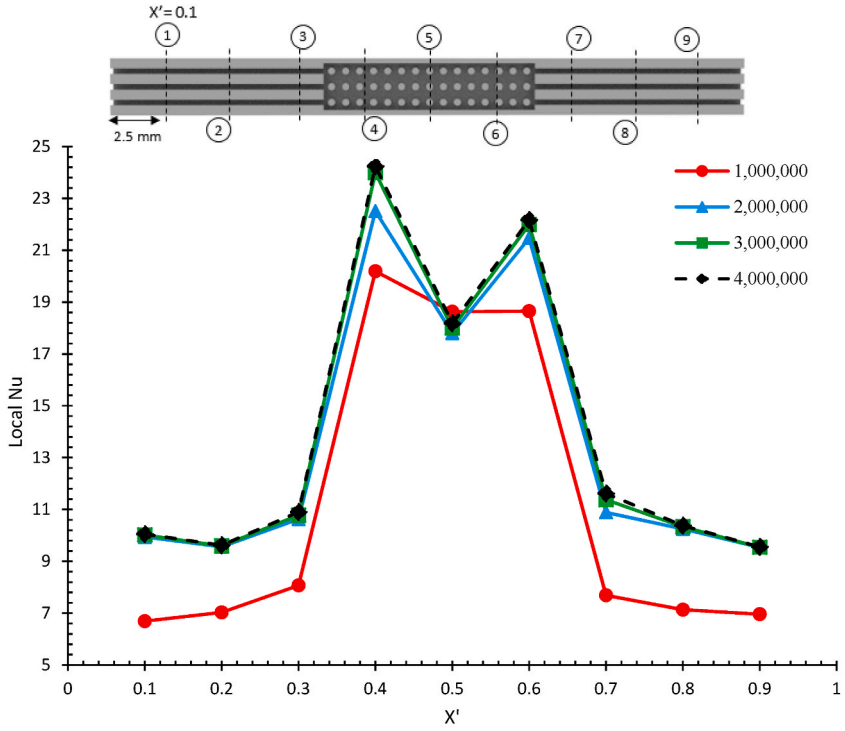

Fig. 5. The investigation of grid independence by local Nusselt number versus the normalized location of microchannel.

obtained to be 571.2 %, 571.2 %, 425.7 %, and 91.5 % higher than that of Case I at a Reynolds number of 650 that are shown in Table 3. This percentage at the Reynolds number of 850 has declined compared to the Reynolds number of 650. Thus, the proposed models could significantly enhance the Nusselt number. The maximum Nusselt number occurred to be nearly 61 for Case V and Case IV at a Reynolds number of 1250, followed by Case II with a Nusselt number of 45.

According to Table 4, it can be concluded that heat transfer is directly related to the flow-wetted area; Case V and Case IV, with the largest wetted areas, had the highest heat transfer. However, despite their greater wetted areas, Case III and Case I had a lower heat transfer rate than Case II since the straight design thermal boundary conditions were not destroyed. Furthermore, the enhanced heat transfer can be explained by the fact that the proposed models kept the flow regime developing, enabled the periodic growth of thermal boundary layers, and imposed flow barriers, increasing flow-wall mixing and improving the heat transfer rate.

4.2. Flow and temperature characterization

4.2.1. Temperature contours

As previously discussed, an increase in the Reynolds number corresponds to a rise in the Nusselt number. Fig. 8 depicts temperature contours, both longitudinal and transverse, at a Reynolds number of 1250, focusing on three evenly spaced transverse sections along

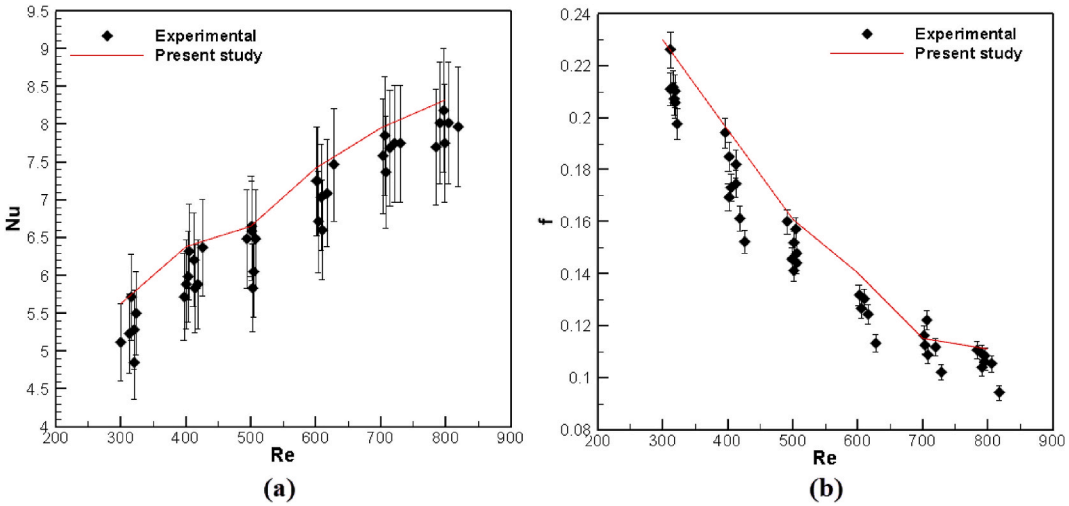

Fig. 6. The comparison of Nusselt number (a) and friction factor (b) calculated in the present study with the experimental study of Sui et al. for different Reynolds numbers [32].

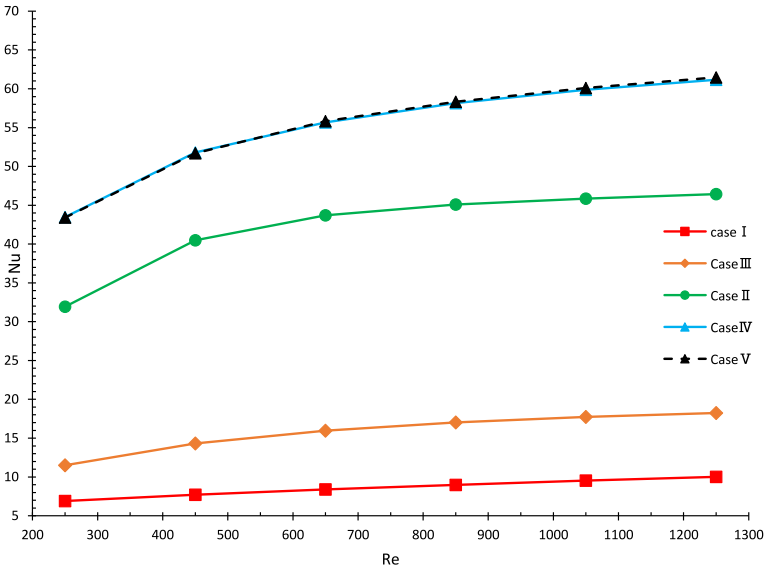

Fig. 7. Nusselt number variations at different Reynolds numbers for all the cases.

Table 3
The relative difference of the Nusselt numbers for Case V, Case IV, Case III, and Case II versus Case I in terms of percent at the different Reynolds number.

Re	$\left[\frac{(Nu_{CaseV}-Nu_{CaseI})}{Nu_{CaseI}}\right]\times 100$	$\left[\frac{(Nu_{CaseIV}-Nu_{CaseI})}{Nu_{CaseI}}\right]\times 100$	$\left[\frac{(Nu_{CaseIII}-Nu_{CaseI})}{Nu_{CaseI}}\right]\times 100$	$\left[\frac{(Nu_{CaseII}-Nu_{CaseI})}{Nu_{CaseI}}\right]\times 100$
250	536.3 %	536.3 %	66.4 %	366.7 %
450	572.1 %	572.1 %	84.5 %	425.9 %
650	571.2 %	571.2 %	91.5 %	425.7 %
850	545.1 %	545.1 %	86.8 %	398.3 %
1050	538.1 %	538.1 %	87.3 %	386.8 %
1250	525.1 %	517.7 %	83 %	367.3 %

the flow direction. According to Fig. 8, it was expectedly observed that a large portion of the fluid flowed at an unchanged temperature (input temperature) in Case I due to the absence of barriers. The temperature increased when the flow met the channel wall, reaching a maximum of 348 K. For Case II, the heat was efficiently transferred due to the flow barriers, and the temperature consistently increased

Table 4
Variables amount of Ab/Ai for Case I, Case II, Case III, Case IV, and Case V.

Model	A_b*/A_i**		
	Zone 1	Zone 2	Zone 3
Case I	0.74	0.74	0.74
Case II	0.59	0.59	0.59
Case III	0.74	0.59	0.74
Case IV	1.85	0.59	1.85
Case V	1.85	0.59	1.85

* A_b = heat flux-subjected surface area.
** A_i = Available area for convection.

from the inlet to the outlet up to 316 K in some locations. As can be seen, heat transfer was efficient downstream of the fins due to rotational areas. As a combination of straight and pin-fin designs, Case III was found to have the same heat transfer as Case I, except that flow mixing sharply increased in the interface of the two designs due to an abrupt change in the cross-sectional area, where heat was effectively transferred. Then, the fluid flowed through the pin-fins and reached the interface of the pin-fins and straight design, heat transfer occurred efficiently, with a sharp change in the cross-sectional area. Therefore, it can be said that Case III had higher heat transfer than Case I, partially due to the use of pin-fins for further flow mixing. However, both Case III and Case I had lower heat transfer than Case II. For Case IV and Case V, which combine grooves and pin-fins, the inclusion of grooves notably enhanced heat transfer. The inlet grooves enhanced flow mixing and thermal performance.

As the flow reached the pin-fin area, the fluid temperature increased compared to Case II due to a sharp change in the cross-sectional area and improved flow mixing. Comparing Case II, Case III, Case IV, and Case V indicates that pin-fin cooling was symmetric in Case II and Case III, while such symmetric is lacking in Case IV and Case V due to upstream grooves. The only difference between Case IV and Case V lies in the opposite groove direction downstream of the flow. It can be said that Case V had a more effective cooling performance than Case IV since the upstream grooves were positioned opposite to the downstream grooves. The lower cooling temperature is another advantage of Case V over Case IV; under the same conditions, the flow temperature of Case V was found to be 1 K lower than Case IV (i.e., 321 K). Table 5 reports the temperature difference between the bottom surface of the heat sink and flow at a Reynolds number of 1250. A more negligible temperature difference implies a more effective heat transfer rate. According to Table 5, the lowest temperature difference was observed to occur in Case V and Case IV, followed by Case II.

4.2.2. *Velocity contours*

The velocity distribution was evaluated and related to heat transfer. Fig. 9 plots the velocity distributions in the longitudinal section and three transverse sections of the same spacing. According to Fig. 9, the velocity boundary layer increased in Case I. Due to the absence of barriers, the boundary layers met almost the middle of the channel. Then, the velocity remained unchanged.

Consequently, the reduced cooling capacity can be linked to the continuous growth and persistence of these boundary layers. Additionally, it was observed that no secondary flow contributed to flow mixing formed in the transverse section. In Case II, the fin pins facilitated flow mixing between the fins and the wall, effectively disrupting the boundary layer. Also, open rotational flow areas formed downstream of the flow (observable in the longitudinal section). These areas substantially contribute to heat transfer. Besides, secondary flows are evident in the transverse sections. These secondary flows, transitioning into a rotational pattern in the transverse section, intensify flow mixing and reach a peak velocity of 11 m/s. For Case III, flow mixing increased in the interface of the pin-fins and straight channels due to a sharp cross-sectional area change, and the flow remained developing in the straight channels.

Unlike Case I, there was no formation of secondary flow. Secondary flows emerged due to flow mixing at the interface of pin-fins and straight channels, leading to the gradual growth of boundary layers. As a result, the heat transfer exceeded that of Case I. In Case IV and Case V, grooves disrupted the flow both upstream and downstream, leading to the formation of secondary solid flows based on the groove configuration. Consequently, Case IV and Case V exhibited stronger flow-wall interactions compared to other models, resulting in enhanced flow mixing within the transverse channels or grooves. As illustrated in Fig. 10, the downstream grooves are oriented in opposite directions for the inlet and outlet. As seen, Case V had a 1 K lower cooling temperature than Case IV, as with the temperature distribution plots. The upward direction of the inlet grooves led to higher cooling at the top of the channel. Thus, the outlet grooves were positioned opposite the inlet to obtain symmetric cooling and avoid hot spots. As a result, the heat sink has a uniform temperature and flow distribution. It transfers heat uniformly in cooling electronic devices, such as CPUs, avoiding hot spots. As mentioned, Case IV and Case V have almost the same temperature distribution, with a temperature difference of 1 K. However, Case IV potentially extends the service life of electronic devices by preventing hot spots.

4.3. *Pressure drop*

Pressure drop serves as a crucial metric in evaluating heat sink performance. Fig. 11 plots the pressure drop versus the Reynolds number. The pressure drop was expected to rise as the Reynolds number increased in all the models. Notably, the rate of change in pressure drops for Case II, Case IV, and Case V surpassed that of Case I and Case III when Reynolds numbers exceeded 700. This can be explained by an increased flow rate (increased Reynolds number) and raised flow-wall mixing, exponentially raising the pressure drop in Case II, Case IV, and Case V. Specifically, at a Reynolds number of 1050, the pressure drops for Case III, Case II, Case IV, and Case V were 39.3 %, 137.9 %, 147.2 %, and 150.3 % greater, respectively, than that of the straight microchannel model, Case I. Also, the maximum pressure drops occurred in Case IV and Case V (i.e., 130 kPa at $Re = 1250$). Thus, Case IV and Case V experienced the most

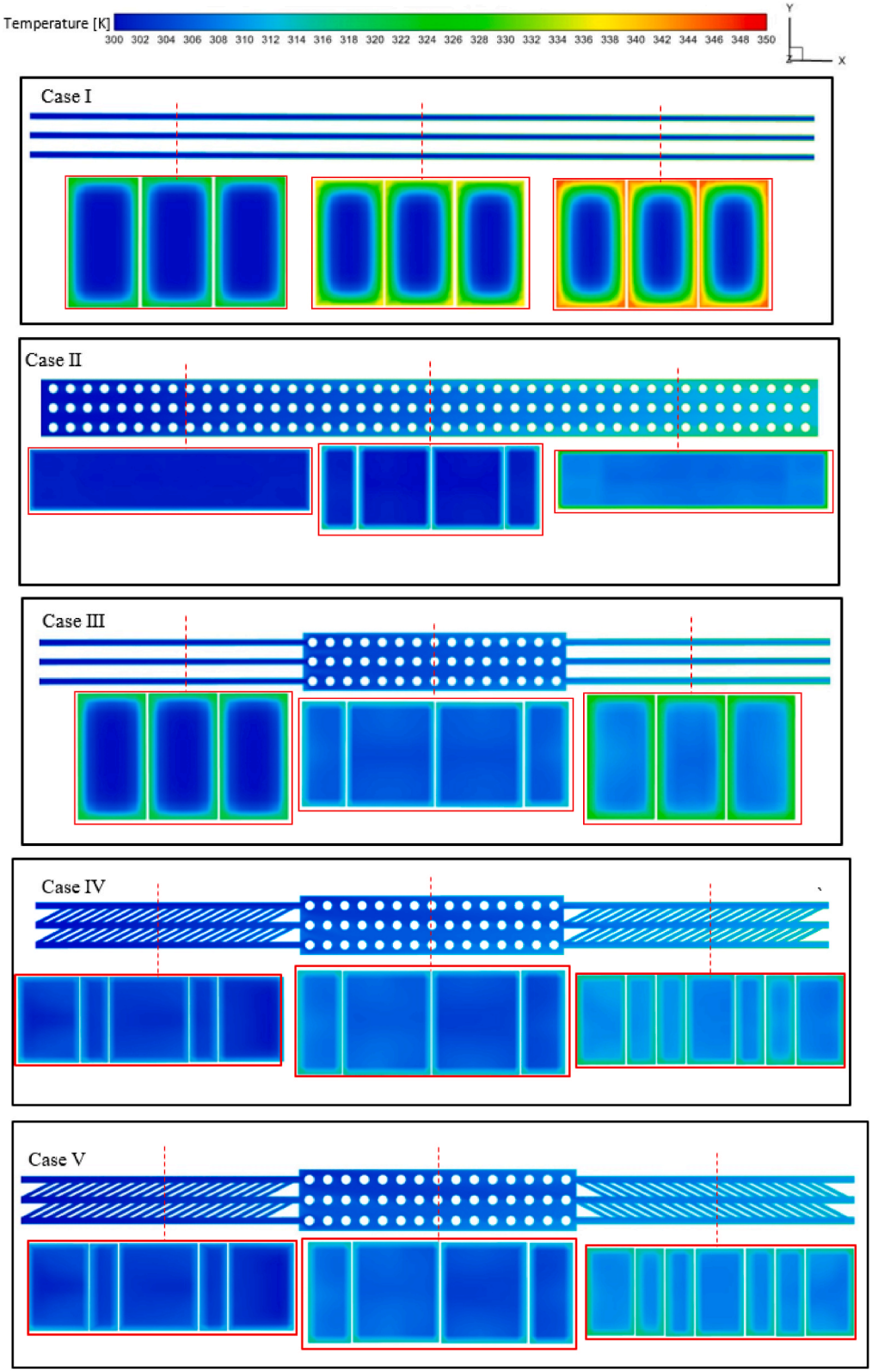

Fig. 8. The temperature contours in three transverse sections, which are located in $x' = 0.2,0.5$ and 0.8 at *Re*: 1250 for all the cases.

Table 5
The temperature difference between the bottom surface of the heat sink and flow for five models at a Reynolds number of 1250.

Model	Average T_w-T_f ($Re = 1250$)
Case I	24.33
Case II	8.17
Case III	13.46
Case IV	7.61
Case V	7.61

significant pressure drops, followed by Case II. The pronounced pressure drop within the grooves can be ascribed to their narrower width, which offers limited pathways for fluid flow.

Moreover, the pumping power supplied to microchannel is obtained as follows:

$$P_{pumping\ power} = \frac{\dot{m}}{\rho_{fluid}} \Delta P \tag{13}$$

Where ρ, and ΔP are the density and pressure drop of flow, respectively. Pumping power for all cases at $Re = 1250$ is presented in Table 6. The pumping power has a direct relationship with pressure drop. Therefore, that hybrid patterns (case IV and case V) require higher power consumption to pump the coolant to the microchannel.

4.4. Performance evaluation index

The introduced pin-fin and groove models demonstrated an increase in both the Nusselt number and pressure drop when compared to the straight model for a specific Reynolds number. Therefore, making a definitive assessment of microchannel efficiency remains challenging. Certain equations were utilized to precisely assess the Nusselt number and the increase in pressure drop. It should be noted that the performance coefficient η, derived by equation (14), accurately measures the performance of a heat sink [33–35].

$$E_{Nu} = \frac{Nu_{\ novel\ pattern}}{Nu_{\ straight}} \tag{14}$$

$$E_{\Delta P} = \frac{\Delta P_{\ novel\ pattern}}{\Delta P_{\ straight}} \tag{15}$$

$$\eta = \frac{E_{Nu}}{\left(E_{\Delta p}\right)^{\frac{1}{3}}} \tag{16}$$

Fig. 12 illustrates a comparison of the performance coefficients for the models across various Reynolds numbers. From the figure, it is evident that Case IV and Case V possess the top performance coefficients. Meanwhile, Case II and Case III rank second and third in terms of performance coefficients. Additionally, for all the introduced models, the performance coefficient exceeded 1. This suggests increased heat transfer had a greater weight than increased pressure drop. Furthermore, for Reynolds numbers exceeding 600, the rate of change in the performance coefficient was more pronounced in Case IV and Case V, suggesting that these cases experience more substantial pressure drops at elevated Reynolds numbers.

5. Conclusion and future directions

This research presents a novel assessment of integrating pin-fins and microchannels across five distinct configurations. Case I consisted of three 25-mm parallel microchannels, while Case II involved three 45-pin-fin arrays (circular pin-fins). The remaining models merge a straight design with pin-fins, characterized by three straight microchannels flanking pin-fins on both ends. Case IV had pin-fins surrounded by 375 μm grooves at the two ends. Case V mirrors Case IV, with the distinction that the grooves at the outlet are oriented in the reverse direction compared to those at the inlet. Simulations were conducted on the copper microchannel and water flow across Reynolds numbers ranging from 250 to 1250, incremented by 200. The findings can be summarized as follows.

- At a Reynolds number of 1250, both Case IV and Case V enhanced the Nusselt number, reaching an approximate value of 61. Additionally, when considering the highest Reynolds number, the Nusselt number in Case V exceeded that of Case I by 525.1 %, in Case IV by 517.7 %, in Case II by 367.3 %, and in Case III by 83 %.
- Enhanced heat transfer in both Case V and Case IV results from a combination of factors: an expanded flow-wetted area, intensified flow-wall interactions, and superior flow mixing within the grooved sections.
- Enhanced heat transfer in the transverse section of the channel is attributed to the expansion of the wetted area and the strength of the secondary flow. Among the cases, Case V and Case IV showcased the most expansive wetted areas and the most pronounced secondary flows, with Case II following closely.
- Case V holds an edge over Case IV due to its superior temperature distribution uniformity and enhanced cooling temperature, a result of the contrasting orientations of the inlet and outlet grooves. At a Reynolds number of 1250, Case V recorded a flow temperature that was 1 K cooler than Case IV, a difference that is expected to widen with increasing Reynolds numbers.

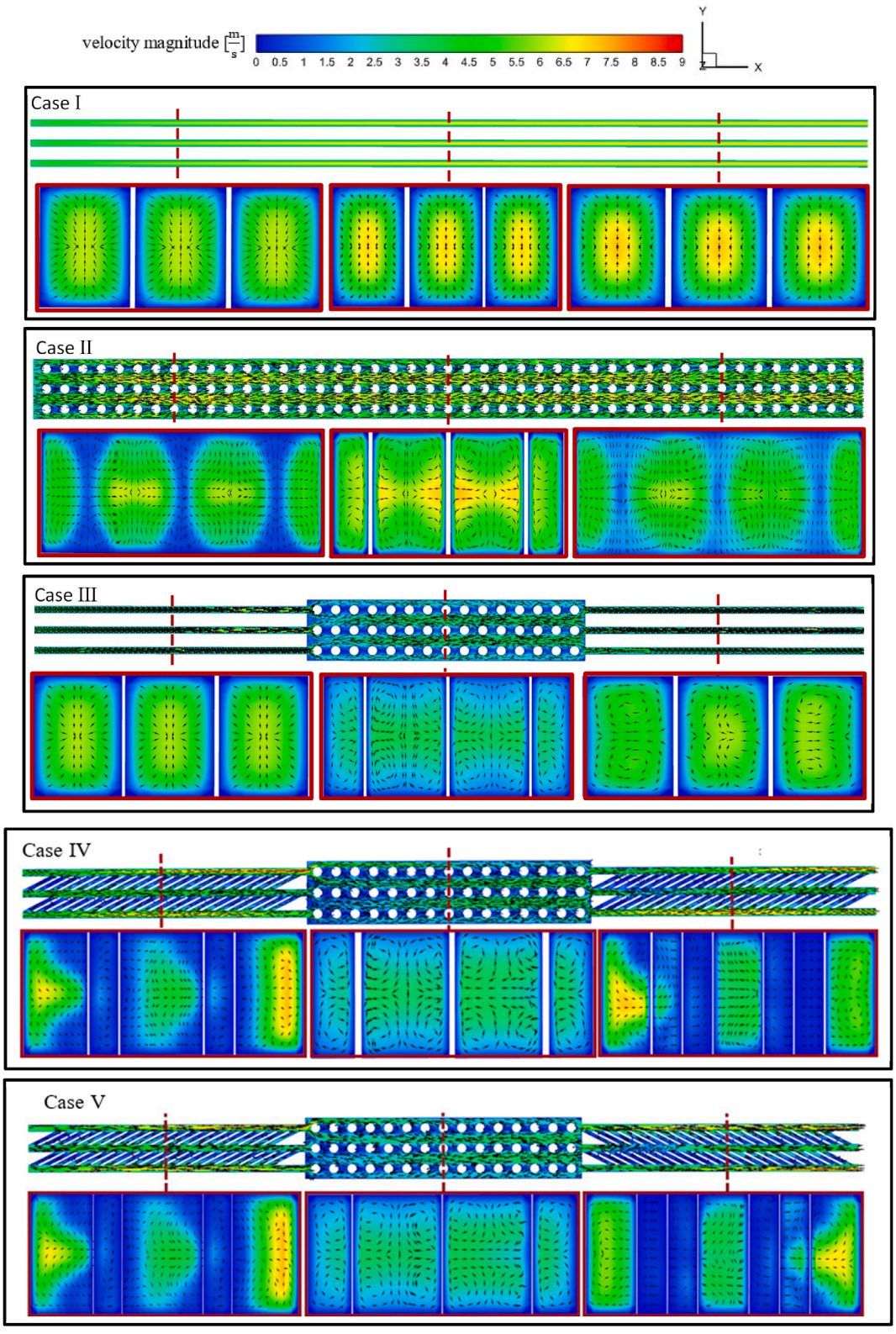

Fig. 9. The velocity distributions in three transverse sections, which are located in $x' = 0.2, 0.5$ and 0.8 at *Re*: 1250 for all the cases.

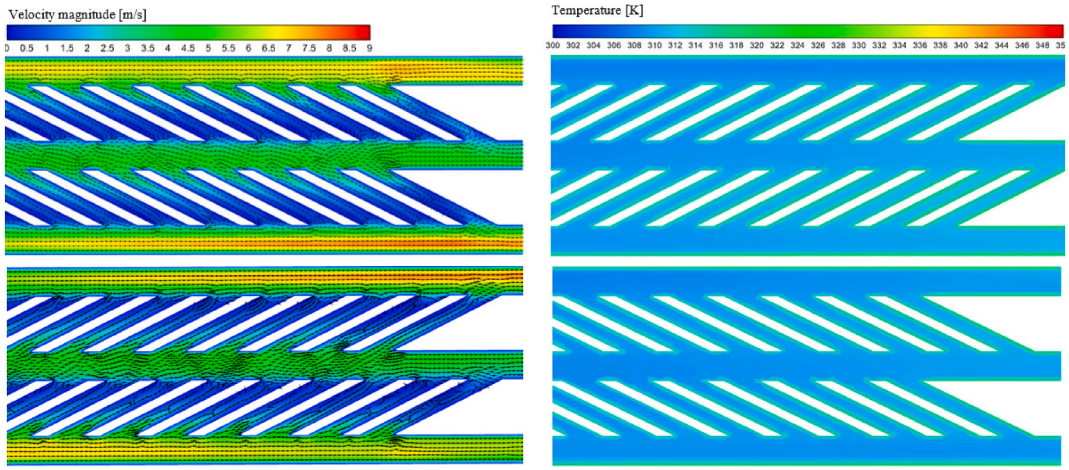

Fig. 10. The velocity and temperature contour for two cases of Case IV and Case V at the downstream flow.

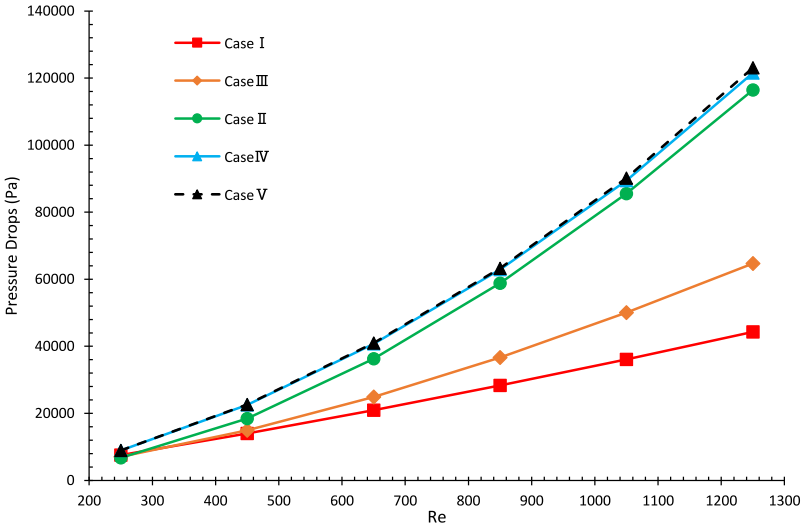

Fig. 11. Pressure drops of five microchannel cases at different Reynolds numbers.

Table 6
The pumping power of flow required for all the cases at $Re = 1250$.

models	$P_{\text{pumping power}}$ (mW)
Case I	44.19
Case II	116.21
Case III	64.56
Case IV	121.26
Case V	122.80

In evaluating the performance of microchannel heat sinks, the pressure drop plays a pivotal role. Both Case V and Case IV experienced more significant pressure drops, a consequence of their transverse grooves and flows. Notably, the peak pressure drops, reaching 130 kPa, were seen in Case IV and Case V, while Case II followed with a pressure drop of 115 kPa. Regarding performance coefficient, the models ranked as follows: Case V, followed by Case IV, Case II, and then Case III. All models yielded performance coefficients exceeding 1, indicating that the benefits of enhanced heat transfer outweighed the drawbacks of increased pressure drop.

Finally, according to the results, some research gaps were recognized, and the following directions are suggested.

- Explore the use of jet impingement as a method to dissipate high heat fluxes.

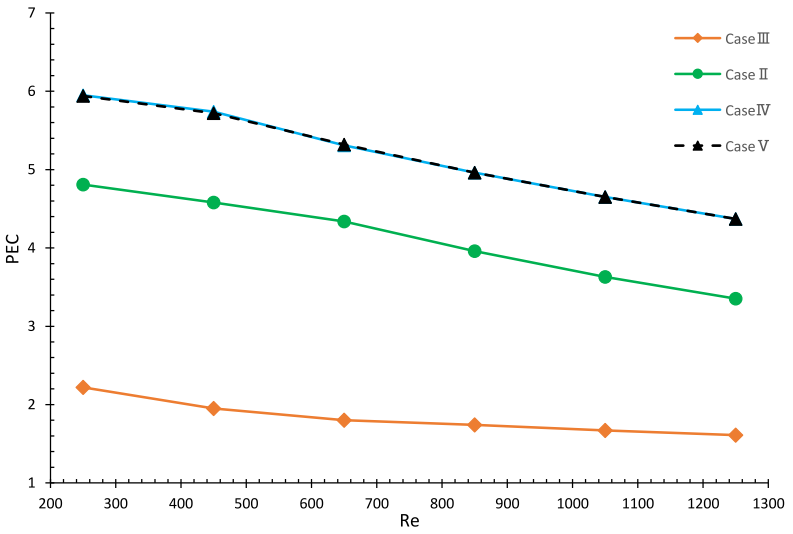

Fig. 12. Performance evaluation criteria index of five cases at different Reynolds numbers.

- Introduce a novel design for MCHS by substituting solid pin-fins with porous ones to increase the heat transfer. Investigating flow, which contains the phase change of particles and hybrid nanofluid in MCHS to enhance thermal performance.

CRediT authorship contribution statement

Yousef Alihosseini: Conceptualization, Project administration, Visualization, Writing – review & editing. **Yaser Oghabneshin:** Software, Visualization, Writing – review & editing. **Amir Rezazad Bari:** Formal analysis, Methodology, Writing – original draft. **Sahel Moslemi:** Validation, Visualization, Writing – review & editing. **Mohammad Zabetian Targhi:** Supervision, Writing – review & editing. **Wei Guo:** Supervision, Writing – review & editing. **Amirarsalan Mashhadian:** Methodology, Software, Validation.

Declaration of competing interest

The authors declare that they have no known competing financial interests or personal relationships that could have appeared to influence the work reported in this paper.

Data availability

No data was used for the research described in the article.

Acknowledgments

Y.A. and W.G. acknowledge the support provided by the National High Magnetic Field Laboratory at Florida State University, which is supported by the National Science Foundation Cooperative Agreement No. DMR-2128556 and the state of Florida.

References

[1] A.H. Khalaj, S.K. Halgamuge, A Review on efficient thermal management of air-and liquid-cooled data centers: from chip to the cooling system, Appl. Energy 205 (2017) 1165–1188.
[2] A. Rajalingam, S. Chakraborty, Microchannel heat sink with microstructured wall—a critical study on fluid flow and heat transfer characteristics, Therm. Sci. Eng. Prog. 38 (2023), 101613.
[3] D.B. Tuckerman, R.F.W. Pease, High-performance heat sinking for VLSI, IEEE Electron. Device Lett. 2 (5) (1981) 126–129.
[4] S.G. Kandlikar, History, advances, and challenges in liquid flow and flow boiling heat transfer in microchannels: a critical review, J. Heat Tran. 134 (3) (2012).
[5] M.R. Haque, R.R. Redu, M.A.-A.A. Rafi, M.M. Haque, M.Z. Rahman, Numerical investigation of heat transfer performance for rectangular, elliptical, and airfoil shaped pin fin heatsinks through the novel combination of perforation and bulge inserts, Int. Commun. Heat Mass Tran. 138 (2022), 106352.
[6] Y. Alihosseini, M.Z. Targhi, M.M. Heyhat, Thermo-hydraulic performance of wavy microchannel heat sink with oblique grooved finned, Appl. Therm. Eng. 189 (2021), 116719.
[7] L. Chai, R. Shaukat, L. Wang, H.S. Wang, A review on heat transfer and hydrodynamic characteristics of nano/microencapsulated phase change slurry (N/MPCS) in mini/microchannel heat sinks, Appl. Therm. Eng. 135 (2018) 334–349.
[8] H.M. Maghrabie, A. Olabi, E.T. Sayed, T. Wilberforce, K. Elsaid, M.H. Doranehgard, M.A. Abdelkareem, Microchannel heat sinks with nanofluids for cooling of electronic components: performance enhancement, challenges, and limitations, Therm. Sci. Eng. Prog. (2022), 101608.
[9] W.M.A.A. Japar, N.A.C. Sidik, R. Saidur, Y. Asako, S.N.A. Yusof, A review of passive methods in microchannel heat sink application through advanced geometric structure and nanofluids: current advancements and challenges, Nanotechnol. Rev. 9 (1) (2020) 1192–1216.
[10] N. Ghorbani, M.Z. Targhi, M.M. Heyhat, Y. Alihosseini, Investigation of wavy microchannel ability on electronic devices cooling with the case study of choosing the most efficient microchannel pattern, Sci. Rep. 12 (1) (2022) 1–21.

[11] M. Khoshvaght-Aliabadi, F. Nozan, Water cooled corrugated minichannel heat sink for electronic devices: effect of corrugation shape, Int. Commun. Heat Mass Tran. 76 (2016) 188–196.
[12] M. Khoshvaght-Aliabadi, S.M. Hassani, S.H. Mazloumi, M. Nekoei, Effects of nooks configuration on hydrothermal performance of zigzag channels for nanofluid-cooled microelectronic heat sink, Microelectron. Reliab. 79 (2017) 153–165.
[13] A. Rezazad Bari, M. Zabetian Targhi, M.M. Heyhat, A numerical study on thermo-hydraulic performance of micro pin-fin heat sink using hybrid pin-fins arrangement for electronic cooling devices, Int. J. Numer. Methods Heat Fluid Flow 33 (7) (2023) 2478–2508.
[14] D. Sahel, L. Bellahcene, A. Yousfi, A. Subasi, Numerical investigation and optimization of a heat sink having hemispherical pin fins, Int. Commun. Heat Mass Tran. 122 (2021), 105133.
[15] M.I. Hasan, Investigation of flow and heat transfer characteristics in micro pin fin heat sink with nanofluid, Appl. Therm. Eng. 63 (2) (2014) 598–607.
[16] T. Ambreen, M.-H. Kim, Effect of fin shape on the thermal performance of nanofluid-cooled micro pin-fin heat sinks, Int. J. Heat Mass Tran. 126 (2018) 245–256.
[17] T. Ambreen, A. Saleem, C.W. Park, Pin-fin shape-dependent heat transfer and fluid flow characteristics of water-and nanofluid-cooled micropin-fin heat sinks: square, circular and triangular fin cross-sections, Appl. Therm. Eng. 158 (2019), 113781.
[18] W. Duangthongsuk, S. Wongwises, A comparison of the heat transfer performance and pressure drop of nanofluid-cooled heat sinks with different miniature pin fin configurations, Exp. Therm. Fluid Sci. 69 (2015) 111–118.
[19] Y.-J. Lee, P.-S. Lee, S.-K. Chou, Enhanced Microchannel Heat Sinks Using Oblique Fins, pp. 253-260..
[20] Y.J. Lee, P.S. Lee, S.K. Chou, Enhanced thermal transport in microchannel using oblique fins, J. Heat Tran. 134 (10) (2012).
[21] Y.J. Lee, P.K. Singh, P.S. Lee, Fluid flow and heat transfer investigations on enhanced microchannel heat sink using oblique fins with parametric study, Int. J. Heat Mass Tran. 81 (2015) 325–336.
[22] Y. Alihosseini, Geometrical Design and Experimental Investigation of Microchannel Heat Sink Aimed at Performance Improvement, Mechanical Engineering, Tarbiat Modares University, Tarbiat Modares University, 2020.
[23] N. Ghorbani, Experimental Study on the Effect of Design Parameters and Governing Phenomena of Particulate Flow on Heat Transfer of Microchannels, Mechanical Engineering, Tarbiat Modares University, Tarbiat Modares University, 2019.
[24] Y. Sui, C.J. Teo, P.S. Lee, Y.T. Chew, C. Shu, Fluid flow and heat transfer in wavy microchannels, Int. J. Heat Mass Tran. 53 (13–14) (2010) 2760–2772.
[25] Y. Alihosseini, A.R. Bari, M. Mohammadi, Effective parameters on increasing efficiency of microscale heat sinks and application of liquid cooling in real life, Adv. Microfluid. Nanofluid. (2021) 155–178.
[26] B. Fani, M. Kalteh, A. Abbassi, Investigating the effect of Brownian motion and viscous dissipation on the nanofluid heat transfer in a trapezoidal microchannel heat sink, Adv. Powder Technol. 26 (1) (2015) 83–90.
[27] N.R. Kuppusamy, R. Saidur, N.N.N. Ghazali, H.A. Mohammed, Numerical study of thermal enhancement in micro channel heat sink with secondary flow, Int. J. Heat Mass Tran. 78 (2014) 216–223.
[28] C.L. Chapman, S. Lee, B.L. Schmidt, Thermal Performance of an Elliptical Pin Fin Heat Sink, IEEE, pp. 24-31..
[29] L. Chen, D. Deng, Q. Ma, Y. Yao, X. Xu, Performance evaluation of high concentration photovoltaic cells cooled by microchannels heat sink with serpentine reentrant microchannels, Appl. Energy 309 (2022), 118478.
[30] H. Nemati, M. Moghimi, J. Meyer, Shape optimisation of wavy mini-channel heat sink, Int. Commun. Heat Mass Tran. 122 (2021), 105172.
[31] D.D. Pollock, Physical Properties of Materials for Engineers, vol. 3, CRC press, 2018.
[32] Y. Sui, P. Lee, C. Teo, An experimental study of flow friction and heat transfer in wavy microchannels with rectangular cross section, Int. J. Therm. Sci. 50 (12) (2011) 2473–2482.
[33] R.L. Webb, Performance evaluation criteria for use of enhanced heat transfer surfaces in heat exchanger design, Int. J. Heat Mass Tran. 24 (4) (1981) 715–726.
[34] P. Samira, Z.H. Saeed, S. Motahare, K. Mostafa, Pressure drop and thermal performance of CuO/ethylene glycol (60%)-water (40%) nanofluid in car radiator, Kor. J. Chem. Eng. 32 (4) (2015) 609–616.
[35] M. Rakhsha, F. Akbaridoust, A. Abbassi, S.-A. Majid, Experimental and numerical investigations of turbulent forced convection flow of nano-fluid in helical coiled tubes at constant surface temperature, Powder Technol. 283 (2015) 178–189.